First measurement of $e^+e^- \to pK^0_S\bar{n}K^- + \text{c.c.}$ above open charm threshold

M. Ablikim,[1] M. N. Achasov,[10,d] S. Ahmed,[15] M. Albrecht,[4] M. Alekseev,[55a,55c] A. Amoroso,[55a,55c] F. F. An,[1] Q. An,[52,42] J. Z. Bai,[1] Y. Bai,[41] O. Bakina,[27] R. Baldini Ferroli,[23a] Y. Ban,[35] K. Begzsuren,[25] D. W. Bennett,[22] J. V. Bennett,[5] N. Berger,[26] M. Bertani,[23a] D. Bettoni,[24a] F. Bianchi,[55a,55c] E. Boger,[27,b] I. Boyko,[27] R. A. Briere,[5] H. Cai,[57] X. Cai,[1,42] O. Cakir,[45a] A. Calcaterra,[23a] G. F. Cao,[1,46] S. A. Cetin,[45b] J. Chai,[55c] J. F. Chang,[1,42] G. Chelkov,[27,b,c] G. Chen,[1] H. S. Chen,[1,46] J. C. Chen,[1] M. L. Chen,[1,42] P. L. Chen,[53] S. J. Chen,[33] X. R. Chen,[30] Y. B. Chen,[1,42] W. Cheng,[55c] X. K. Chu,[35] G. Cibinetto,[24a] F. Cossio,[55c] H. L. Dai,[1,42] J. P. Dai,[37,h] A. Dbeyssi,[15] D. Dedovich,[27] Z. Y. Deng,[1] A. Denig,[26] I. Denysenko,[27] M. Destefanis,[55a,55c] F. De Mori,[55a,55c] Y. Ding,[31] C. Dong,[34] J. Dong,[1,42] L. Y. Dong,[1,46] M. Y. Dong,[1,42,46] Z. L. Dou,[33] S. X. Du,[60] P. F. Duan,[1] J. Fang,[1,42] S. S. Fang,[1,46] Y. Fang,[1] R. Farinelli,[24a,24b] L. Fava,[55b,55c] S. Fegan,[26] F. Feldbauer,[4] G. Felici,[23a] C. Q. Feng,[52,42] E. Fioravanti,[24a] M. Fritsch,[4] C. D. Fu,[1] Q. Gao,[1] X. L. Gao,[52,42] Y. Gao,[44] Y. G. Gao,[6] Z. Gao,[52,42] B. Garillon,[26] I. Garzia,[24a] A. Gilman,[49] K. Goetzen,[11] L. Gong,[34] W. X. Gong,[1,42] W. Gradl,[26] M. Greco,[55a,55c] L. M. Gu,[33] M. H. Gu,[1,42] Y. T. Gu,[13] A. Q. Guo,[1] L. B. Guo,[32] R. P. Guo,[1,46] Y. P. Guo,[26] A. Guskov,[27] Z. Haddadi,[29] S. Han,[57] X. Q. Hao,[16] F. A. Harris,[47] K. L. He,[1,46] X. Q. He,[51] F. H. Heinsius,[4] T. Held,[4] Y. K. Heng,[1,42,46] Z. L. Hou,[1] H. M. Hu,[1,46] J. F. Hu,[37,h] T. Hu,[1,42,46] Y. Hu,[1] G. S. Huang,[52,42] J. S. Huang,[16] X. T. Huang,[36] X. Z. Huang,[33] Z. L. Huang,[31] T. Hussain,[54] W. Ikegami Andersson,[56] M. Irshad,[52,42] Q. Ji,[1] Q. P. Ji,[16] X. B. Ji,[1,46] X. L. Ji,[1,42] X. S. Jiang,[1,42,46] X. Y. Jiang,[34] J. B. Jiao,[36] Z. Jiao,[18] D. P. Jin,[1,42,46] S. Jin,[1,46] Y. Jin,[48] T. Johansson,[56] A. Julin,[49] N. Kalantar-Nayestanaki,[29] X. S. Kang,[34] M. Kavatsyuk,[29] B. C. Ke,[1] I. K. Keshk,[4] T. Khan,[52,42] A. Khoukaz,[50] P. Kiese,[26] R. Kiuchi,[1] R. Kliemt,[11] L. Koch,[28] O. B. Kolcu,[45b,f] B. Kopf,[4] M. Kornicer,[47] M. Kuemmel,[4] M. Kuessner,[4] A. Kupsc,[56] M. Kurth,[1] W. Kühn,[28] J. S. Lange,[28] P. Larin,[15] L. Lavezzi,[55c] S. Leiber,[4] H. Leithoff,[26] C. Li,[56] Cheng Li,[52,42] D. M. Li,[60] F. Li,[1,42] F. Y. Li,[35] G. Li,[1] H. B. Li,[1,46] H. J. Li,[1,46] J. C. Li,[1] J. W. Li,[40] K. J. Li,[43] Kang Li,[14] Ke Li,[1] Lei Li,[3] P. L. Li,[52,42] P. R. Li,[46,7] Q. Y. Li,[36] T. Li,[36] W. D. Li,[1,46] W. G. Li,[1] X. L. Li,[36] X. N. Li,[1,42] X. Q. Li,[34] Z. B. Li,[43] H. Liang,[52,42] Y. F. Liang,[39] Y. T. Liang,[28] G. R. Liao,[12] L. Z. Liao,[1,46] J. Libby,[21] C. X. Lin,[43] D. X. Lin,[15] B. Liu,[37,h] B. J. Liu,[1] C. X. Liu,[1] D. Liu,[52,42] D. Y. Liu,[37,h] F. H. Liu,[38] Fang Liu,[1] Feng Liu,[6] H. B. Liu,[13] H. L. Liu,[41] H. M. Liu,[1,46] Huanhuan Liu,[1] Huihui Liu,[17] J. B. Liu,[52,42] J. Y. Liu,[1,46] K. Y. Liu,[31] Ke Liu,[6] L. D. Liu,[35] Q. Liu,[46] S. B. Liu,[52,42] X. Liu,[30] Y. B. Liu,[34] Z. A. Liu,[1,42,46] Zhiqing Liu,[26] Y. F. Long,[35] X. C. Lou,[1,42,46] H. J. Lu,[18] J. G. Lu,[1,42] Y. Lu,[1] Y. P. Lu,[1,42] C. L. Luo,[32] M. X. Luo,[59] T. Luo,[9,j] X. L. Luo,[1,42] S. Lusso,[55c] X. R. Lyu,[46] F. C. Ma,[31] H. L. Ma,[1] L. L. Ma,[36] M. M. Ma,[1,46] Q. M. Ma,[1] T. Ma,[1] X. N. Ma,[34] X. Y. Ma,[1,42] Y. M. Ma,[36] F. E. Maas,[15] M. Maggiora,[55a,55c] S. Maldaner,[26] Q. A. Malik,[54] A. Mangoni,[23b] Y. J. Mao,[35] Z. P. Mao,[1] S. Marcello,[55a,55c] Z. X. Meng,[48] J. G. Messchendorp,[29] G. Mezzadri,[24b] J. Min,[1,42] T. J. Min,[33] R. E. Mitchell,[22] X. H. Mo,[1,42,46] Y. J. Mo,[6] C. Morales Morales,[15] N. Yu. Muchnoi,[10,d] H. Muramatsu,[49] A. Mustafa,[4] S. Nakhoul,[11,g] Y. Nefedov,[27] F. Nerling,[11] I. B. Nikolaev,[10,d] Z. Ning,[1,42] S. Nisar,[8] S. L. Niu,[1,42] X. Y. Niu,[1,46] S. L. Olsen,[46] Q. Ouyang,[1,42,46] S. Pacetti,[23b] Y. Pan,[52,42] M. Papenbrock,[56] P. Patteri,[23a] M. Pelizaeus,[4] J. Pellegrino,[55a,55c] H. P. Peng,[52,42] Z. Y. Peng,[13] K. Peters,[11,g] J. Pettersson,[56] J. L. Ping,[32] R. G. Ping,[1,46] A. Pitka,[4] R. Poling,[49] V. Prasad,[52,42] H. R. Qi,[2,*] M. Qi,[33] T. Y. Qi,[2] S. Qian,[1,42] C. F. Qiao,[46] N. Qin,[57] X. S. Qin,[4] Z. H. Qin,[1,42] J. F. Qiu,[1] S. Q. Qu,[34] K. H. Rashid,[54,i] C. F. Redmer,[26] M. Richter,[4] M. Ripka,[26] A. Rivetti,[55c] M. Rolo,[55c] G. Rong,[1,46] Ch. Rosner,[15] A. Sarantsev,[27,e] M. Savrié,[24b] K. Schoenning,[56] W. Shan,[19] X. Y. Shan,[52,42] M. Shao,[52,42] C. P. Shen,[2] P. X. Shen,[34] X. Y. Shen,[1,46] H. Y. Sheng,[1] X. Shi,[1,42] J. J. Song,[36] W. M. Song,[36] X. Y. Song,[1] S. Sosio,[55a,55c] C. Sowa,[4] S. Spataro,[55a,55c] G. X. Sun,[1] J. F. Sun,[16] L. Sun,[57] S. S. Sun,[1,46] X. H. Sun,[1] Y. J. Sun,[52,42] Y. K. Sun,[52,42] Y. Z. Sun,[1] Z. J. Sun,[1,42] Z. T. Sun,[1] Y. T. Tan,[52,42] C. J. Tang,[39] G. Y. Tang,[1] X. Tang,[1] I. Tapan,[45c] M. Tiemens,[29] B. Tsednee,[25] I. Uman,[45d] B. Wang,[1] B. L. Wang,[46] C. W. Wang,[33] D. Wang,[35] D. Y. Wang,[35] Dan Wang,[46] K. Wang,[1,42] L. L. Wang,[1] L. S. Wang,[1] M. Wang,[36] Meng Wang,[1,46] P. Wang,[1] P. L. Wang,[1] W. P. Wang,[52,42] X. F. Wang,[44] Y. Wang,[52,42] Y. F. Wang,[1,42,46] Z. Wang,[1,42] Z. G. Wang,[1,42] Z. Y. Wang,[1] Zongyuan Wang,[1,46] T. Weber,[4] D. H. Wei,[12] P. Weidenkaff,[26] S. P. Wen,[1] U. Wiedner,[4] M. Wolke,[56] L. H. Wu,[1] L. J. Wu,[1,46] Z. Wu,[1,42] L. Xia,[52,42] X. Xia,[36] Y. Xia,[20] D. Xiao,[1] Y. J. Xiao,[1,46] Z. J. Xiao,[32] Y. G. Xie,[1,42] Y. H. Xie,[6] X. A. Xiong,[1,46] Q. L. Xiu,[1,42] G. F. Xu,[1] J. J. Xu,[1,46] L. Xu,[1] Q. J. Xu,[14] X. P. Xu,[40] F. Yan,[53] L. Yan,[55a,55c] W. B. Yan,[52,42] W. C. Yan,[2] Y. H. Yan,[20] H. J. Yang,[37,h] H. X. Yang,[1] L. Yang,[57] R. X. Yang,[52,42] Y. H. Yang,[33] Y. X. Yang,[12] Yifan Yang,[1,46] Z. Q. Yang,[20] M. Ye,[1,42] M. H. Ye,[7] J. H. Yin,[1] Z. Y. You,[43] B. X. Yu,[1,42,46] C. X. Yu,[34] J. S. Yu,[20] J. S. Yu,[30] C. Z. Yuan,[1,46] Y. Yuan,[1] A. Yuncu,[45b,a] A. A. Zafar,[54] Y. Zeng,[20] B. X. Zhang,[1] B. Y. Zhang,[1,42] C. C. Zhang,[1] D. H. Zhang,[1] H. H. Zhang,[43] H. Y. Zhang,[1,42] J. Zhang,[1,46] J. L. Zhang,[58] J. Q. Zhang,[4] J. W. Zhang,[1,42,46] J. Y. Zhang,[1] J. Z. Zhang,[1,46] K. Zhang,[1,46] L. Zhang,[44] S. F. Zhang,[33] T. J. Zhang,[37,h] X. Y. Zhang,[36] Y. Zhang,[52,42] Y. H. Zhang,[1,42] Y. T. Zhang,[52,42] Yang Zhang,[1] Yao Zhang,[1] Yu Zhang,[46] Z. H. Zhang,[6] Z. P. Zhang,[52] Z. Y. Zhang,[57] G. Zhao,[1] J. W. Zhao,[1,42] J. Y. Zhao,[1,46] J. Z. Zhao,[1,42] Lei Zhao,[52,42] Ling Zhao,[1] M. G. Zhao,[34] Q. Zhao,[1] S. J. Zhao,[60] T. C. Zhao,[1] Y. B. Zhao,[1,42] Z. G. Zhao,[52,42] A. Zhemchugov,[27,b] B. Zheng,[53] J. P. Zheng,[1,42] W. J. Zheng,[36] Y. H. Zheng,[46] B. Zhong,[32] L. Zhou,[1,42] Q. Zhou,[1,46] X. Zhou,[57] X. K. Zhou,[52,42] X. R. Zhou,[52,42] X. Y. Zhou,[1] Xiaoyu Zhou,[20] Xu Zhou,[20]

A. N. Zhu,[1,46] J. Zhu,[34] J. Zhu,[43] K. Zhu,[1] K. J. Zhu,[1,42,46] S. Zhu,[1] S. H. Zhu,[51] X. L. Zhu,[44] Y. C. Zhu,[52,42] Y. S. Zhu,[1,46] Z. A. Zhu,[1,46] J. Zhuang,[1,42] B. S. Zou,[1] and J. H. Zou[1]

(BESIII Collaboration)

[1]*Institute of High Energy Physics, Beijing 100049, People's Republic of China*
[2]*Beihang University, Beijing 100191, People's Republic of China*
[3]*Beijing Institute of Petrochemical Technology, Beijing 102617, People's Republic of China*
[4]*Bochum Ruhr-University, D-44780 Bochum, Germany*
[5]*Carnegie Mellon University, Pittsburgh, Pennsylvania 15213, USA*
[6]*Central China Normal University, Wuhan 430079, People's Republic of China*
[7]*China Center of Advanced Science and Technology, Beijing 100190, People's Republic of China*
[8]*COMSATS Institute of Information Technology, Lahore, Defence Road, Off Raiwind Road, 54000 Lahore, Pakistan*
[9]*Fudan University, Shanghai 200443, People's Republic of China*
[10]*G.I. Budker Institute of Nuclear Physics SB RAS (BINP), Novosibirsk 630090, Russia*
[11]*GSI Helmholtzcentre for Heavy Ion Research GmbH, D-64291 Darmstadt, Germany*
[12]*Guangxi Normal University, Guilin 541004, People's Republic of China*
[13]*Guangxi University, Nanning 530004, People's Republic of China*
[14]*Hangzhou Normal University, Hangzhou 310036, People's Republic of China*
[15]*Helmholtz Institute Mainz, Johann-Joachim-Becher-Weg 45, D-55099 Mainz, Germany*
[16]*Henan Normal University, Xinxiang 453007, People's Republic of China*
[17]*Henan University of Science and Technology, Luoyang 471003, People's Republic of China*
[18]*Huangshan College, Huangshan 245000, People's Republic of China*
[19]*Hunan Normal University, Changsha 410081, People's Republic of China*
[20]*Hunan University, Changsha 410082, People's Republic of China*
[21]*Indian Institute of Technology Madras, Chennai 600036, India*
[22]*Indiana University, Bloomington, Indiana 47405, USA*
[23a]*INFN Laboratori Nazionali di Frascati, I-00044, Frascati, Italy*
[23b]*INFN and University of Perugia, I-06100, Perugia, Italy*
[24a]*INFN Sezione di Ferrara, I-44122, Ferrara, Italy*
[24b]*University of Ferrara, I-44122, Ferrara, Italy*
[25]*Institute of Physics and Technology, Peace Ave. 54B, Ulaanbaatar 13330, Mongolia*
[26]*Johannes Gutenberg University of Mainz, Johann-Joachim-Becher-Weg 45, D-55099 Mainz, Germany*
[27]*Joint Institute for Nuclear Research, 141980 Dubna, Moscow region, Russia*
[28]*Justus-Liebig-Universitaet Giessen, II. Physikalisches Institut, Heinrich-Buff-Ring 16, D-35392 Giessen, Germany*
[29]*KVI-CART, University of Groningen, NL-9747 AA Groningen, Netherlands*
[30]*Lanzhou University, Lanzhou 730000, People's Republic of China*
[31]*Liaoning University, Shenyang 110036, People's Republic of China*
[32]*Nanjing Normal University, Nanjing 210023, People's Republic of China*
[33]*Nanjing University, Nanjing 210093, People's Republic of China*
[34]*Nankai University, Tianjin 300071, People's Republic of China*
[35]*Peking University, Beijing 100871, People's Republic of China*
[36]*Shandong University, Jinan 250100, People's Republic of China*
[37]*Shanghai Jiao Tong University, Shanghai 200240, People's Republic of China*
[38]*Shanxi University, Taiyuan 030006, People's Republic of China*
[39]*Sichuan University, Chengdu 610064, People's Republic of China*
[40]*Soochow University, Suzhou 215006, People's Republic of China*
[41]*Southeast University, Nanjing 211100, People's Republic of China*
[42]*State Key Laboratory of Particle Detection and Electronics, Beijing 100049, Hefei 230026, People's Republic of China*
[43]*Sun Yat-Sen University, Guangzhou 510275, People's Republic of China*
[44]*Tsinghua University, Beijing 100084, People's Republic of China*
[45a]*Ankara University, 06100 Tandogan, Ankara, Turkey*
[45b]*Istanbul Bilgi University, 34060 Eyup, Istanbul, Turkey*
[45c]*Uludag University, 16059 Bursa, Turkey*
[45d]*Near East University, Nicosia, North Cyprus, Mersin 10, Turkey*
[46]*University of Chinese Academy of Sciences, Beijing 100049, People's Republic of China*
[47]*University of Hawaii, Honolulu, Hawaii 96822, USA*

[48]University of Jinan, Jinan 250022, People's Republic of China
[49]University of Minnesota, Minneapolis, Minnesota 55455, USA
[50]University of Muenster, Wilhelm-Klemm-Straße 9, 48149 Muenster, Germany
[51]University of Science and Technology Liaoning, Anshan 114051, People's Republic of China
[52]University of Science and Technology of China, Hefei 230026, People's Republic of China
[53]University of South China, Hengyang 421001, People's Republic of China
[54]University of the Punjab, Lahore-54590, Pakistan
[55a]University of Turin, I-10125, Turin, Italy
[55b]University of Eastern Piedmont, I-15121, Alessandria, Italy
[55c]INFN, I-10125, Turin, Italy
[56]Uppsala University, Box 516, SE-75120 Uppsala, Sweden
[57]Wuhan University, Wuhan 430072, People's Republic of China
[58]Xinyang Normal University, Xinyang 464000, People's Republic of China
[59]Zhejiang University, Hangzhou 310027, People's Republic of China
[60]Zhengzhou University, Zhengzhou 450001, People's Republic of China

(Received 10 July 2018; published 28 August 2018)

The process $e^+e^- \to pK_S^0\bar{n}K^- + \text{c.c.}$ and its intermediate processes are studied for the first time, using data samples collected with the BESIII detector at BEPCII at center-of-mass energies of 3.773, 4.008, 4.226, 4.258, 4.358, 4.416, and 4.600 GeV, with a total integrated luminosity of 7.4 fb^{-1}. The Born cross section of $e^+e^- \to pK_S^0\bar{n}K^- + \text{c.c.}$ is measured at each center-of-mass energy, but no significant resonant structure in the measured cross-section line shape between 3.773 and 4.600 GeV is observed. No evident structure is detected in the pK^-, nK_S^0, pK_S^0, nK^+, $p\bar{n}$, or $K_S^0K^-$ invariant mass distributions except for $\Lambda(1520)$. The Born cross sections of $e^+e^- \to \Lambda(1520)\bar{n}K_S^0 + \text{c.c.}$ and $e^+e^- \to \Lambda(1520)\bar{p}K^+ + \text{c.c.}$ are measured, and the 90% confidence level upper limits on the Born cross sections of $e^+e^- \to \Lambda(1520)\bar{\Lambda}(1520)$ are determined at the seven center-of-mass energies. There is an evident difference in line shape and magnitude of the measured cross sections between $e^+e^- \to \Lambda(1520)(\to pK^-)\bar{n}K_S^0$ and $e^+e^- \to pK^-\bar{\Lambda}(1520)(\to \bar{n}K_S^0)$.

DOI: 10.1103/PhysRevD.98.032014

*Corresponding author.
qihongrong@buaa.edu.cn
[a]Also at Bogazici University, 34342 Istanbul, Turkey.
[b]Also at the Moscow Institute of Physics and Technology, Moscow 141700, Russia.
[c]Also at the Functional Electronics Laboratory, Tomsk State University, Tomsk, 634050, Russia.
[d]Also at the Novosibirsk State University, Novosibirsk, 630090, Russia.
[e]Also at the NRC "Kurchatov Institute", PNPI, 188300, Gatchina, Russia.
[f]Also at Istanbul Arel University, 34295 Istanbul, Turkey.
[g]Also at Goethe University Frankfurt, 60323 Frankfurt am Main, Germany.
[h]Also at Key Laboratory for Particle Physics, Astrophysics and Cosmology, Ministry of Education; Shanghai Key Laboratory for Particle Physics and Cosmology; Institute of Nuclear and Particle Physics, Shanghai 200240, People's Republic of China.
[i]Government College Women University, Sialkot - 51310. Punjab, Pakistan.
[j]Key Laboratory of Nuclear Physics and Ion-beam Application (MOE) and Institute of Modern Physics, Fudan University, Shanghai 200443, People's Republic of China.

I. INTRODUCTION

The experimental discovery of unexpected resonances has brought new opportunities to the study of quantum chromodynamics in the charmonium and bottomonium energy regions [1–3]. The state $Y(4260)$ was discovered by the *BABAR* collaboration [4,5] in the initial state radiation (ISR) process $e^+e^- \to \gamma_{\text{ISR}}\pi^+\pi^- J/\psi$ and confirmed by the CLEO [6] and Belle [7] collaborations in the same process. This state was further confirmed by BESIII [8] and again by Belle [9]. Located above the $D\bar{D}$ mass threshold, the $Y(4260)$ with $J^{PC} = 1^{--}$ anomalously couples to the hidden-charm final state $\pi\pi J/\psi$ [10]. The same phenomenon had been observed in other Y states, such as the $Y(4360)$ and $Y(4660)$ [1]. Just recently, BESIII first reported that two structures around 4.22 and 4.39 GeV in e^+e^- line shape strongly couple to $\pi^+D^0D^{*-}$ [11]. These interesting but little-known phenomenons have prompted researchers to focus on this charmoniumlike spectroscopy [1–3].

Light hadron decays of Y states have not been found above 4 GeV, nor have any such decays of charmonium resonances. The continued search for light hadron decays helps further the understanding of the nature of undefined states and charmonium resonances.

In this paper, we report the cross sections of $e^+e^- \to pK_S^0\bar{n}K^- + \text{c.c.}$ and search for possible structures, such as Y states or higher charmonia, in the $e^+e^- \to pK_S^0\bar{n}K^- + \text{c.c.}$ cross section line shape, using data samples with a total integrated luminosity of 7.4 fb^{-1} collected with the BESIII detector at center-of-mass (c.m.) energies between 3.773 and 4.6 GeV. All possible intermediate states in the pK^-, nK_S^0, pK_S^0, nK^+, $p\bar{n}$, and $K_S^0K^-$ invariant mass spectra and charge conjugated modes, such as Λ^*, Σ^*, $a_0(980)^+$, and other excited or exotic states, are searched for in the $e^+e^- \to pK_S^0\bar{n}K^- + \text{c.c.}$ process. However, no significant structures, except for $\Lambda(1520)$, are seen in any of the studied mass spectra. The Born cross sections of $e^+e^- \to \Lambda(1520)\bar{n}K_S^0$ and $\Lambda(1520)\bar{p}K^+ + \text{c.c.}$ are measured. In the following analysis, charged conjugated modes are included unless otherwise indicated. The process $e^+e^- \to pK_S^0\bar{n}K^-$ with all of the potential intermediate states included is denoted as the "$pK_S^0\bar{n}K^-$ mode" hereinafter. Similarly, the processes $e^+e^- \to \Lambda(1520)\bar{n}K_S^0$, $\Lambda(1520)\bar{p}K^+$ and $\Lambda(1520)\bar{\Lambda}(1520)$ are denoted as "$\Lambda(1520)$ modes."

II. EXPERIMENTAL DATA AND MONTE CARLO SIMULATION

The Beijing Electron Positron Collider II (BEPCII) [12], a double-ring electron–positron collider with a peak luminosity of 10^{33} $\text{cm}^{-2}\,\text{s}^{-1}$ at the c.m. energy of 3.770 GeV at a beam current of 0.93 A, operates in the center-of-mass energy region from 2 to 4.6 GeV. The Beijing Spectrometer III (BESIII) [12], which operates at the BEPCII storage ring, covers 93% of 4π solid angle. A small-cell helium-gas-based main drift chamber (MDC) provides charged particle momentum and ionization loss (dE/dx) measurements for charged particle identification (PID). The momentum resolution is better than 0.5% at 1 GeV/c in a magnetic field of 1 T. A plastic scintillator time-of-flight (TOF) system with a time resolution of 80 ps (110 ps) for the barrel (end caps) is utilized for additional charged particle identification. A CsI(Tl) crystal electromagnetic calorimeter obtains a photon energy resolution of 2.5% (5%) at 1 GeV in the barrel (end caps). A resistive-plate-counter muon system provides a position resolution of 2 cm and can detect muon tracks with momenta greater than 0.5 GeV/c.

All data samples used in this analysis are listed in Table I. The c.m. energies are measured using the dimuon process $e^+e^- \to (\gamma_{\text{ISR/FSR}})\mu^+\mu^-$ with an uncertainty of 0.8 MeV [13], and the integrated luminosities are measured with large-angle Bhabha scattering events with an uncertainty of 1.0% [14–16], where FSR denotes final state radiation. The data sets with c.m. energy above 4 GeV are named "XYZ data".

The GEANT4-based [17] Monte Carlo (MC) simulation framework BOOST [18], consisting of event generators, the detector geometry, and detector response, is used to evaluate the detector efficiency, estimate ISR correction, optimize event selection criteria, and analyze backgrounds. The effects of FSR are simulated by the PHOTOS [19] package. Exclusive phase space (PHSP) MC samples for signal modes are modeled with KKMC [20–22] and BESEVTGEN [23,24], which consider ISR effects and beam energy spreads. Seven "inclusive" MC simulated data samples at the different c.m. energies, equivalent to the respective integrated luminosity of each data set, are produced to investigate potential backgrounds. The main known processes and decay modes are generated by BESEVTGEN with cross sections or branching fractions obtained from the Particle Data Group (PDG) [25], and the remaining unmeasured events associated with charmonium decays or open charm processes are generated with LUNDCHARM [23,26], while continuum light hadronic events are generated with PYTHIA [27].

III. DATA ANALYSIS

In this analysis, the n and $\bar{n}$ candidates are not reconstructed, and a partial reconstruction technique is employed to select the signal events of interest, i.e., we reconstruct $p, K_S^0(\to \pi^+\pi^-)$, and K^- only, while $\bar{n}$ is treated as a missing particle. The presence of a $\bar{n}$ is inferred using the mass recoiling against the $pK_S^0K^-$ system, $M^{\text{rec}}(pK_S^0K^-) = \sqrt{(E-\sum E_i)^2-(\sum \vec{P}_i)^2}$ ($i = p,\ K_S^0,\ K^-$), where E is the

TABLE I. The c.m. energy ($\sqrt{s}$), integrated luminosity ($\mathcal{L}$), detection efficiency (ϵ), vacuum polarization ($\frac{1}{|1-\Pi|^2}$) and radiative correction factor ($1+\delta$), number of fitted $\bar{n}$ signal events (N_{sig}) excluding the peaking backgrounds, and Born cross section (σ_{B}) of $e^+e^- \to pK_S^0\bar{n}K^-$ at each energy point. The first uncertainties are statistical and the second systematic.

$\sqrt{s}$ (GeV)	$\mathcal{L}$ (pb^{-1})	ϵ (%)	$\frac{1}{\lvert 1-\Pi\rvert^2}$	$1+\delta$	N_{sig}	σ_{B} (pb)
3.773	2931.8	33.44	1.057	0.881	2317 ± 62	$3.67 \pm 0.10 \pm 0.20$
4.008	482.0	35.30	1.044	0.926	367 ± 24	$3.22 \pm 0.21 \pm 0.17$
4.226	1047.3	37.03	1.056	0.934	718 ± 38	$2.71 \pm 0.14 \pm 0.14$
4.258	825.7	37.26	1.054	0.936	527 ± 30	$2.51 \pm 0.14 \pm 0.14$
4.358	539.8	38.04	1.051	0.952	325 ± 24	$2.29 \pm 0.17 \pm 0.12$
4.416	1028.9	38.51	1.053	0.960	563 ± 32	$2.03 \pm 0.12 \pm 0.12$
4.600	566.9	39.91	1.055	0.967	264 ± 23	$1.65 \pm 0.14 \pm 0.09$

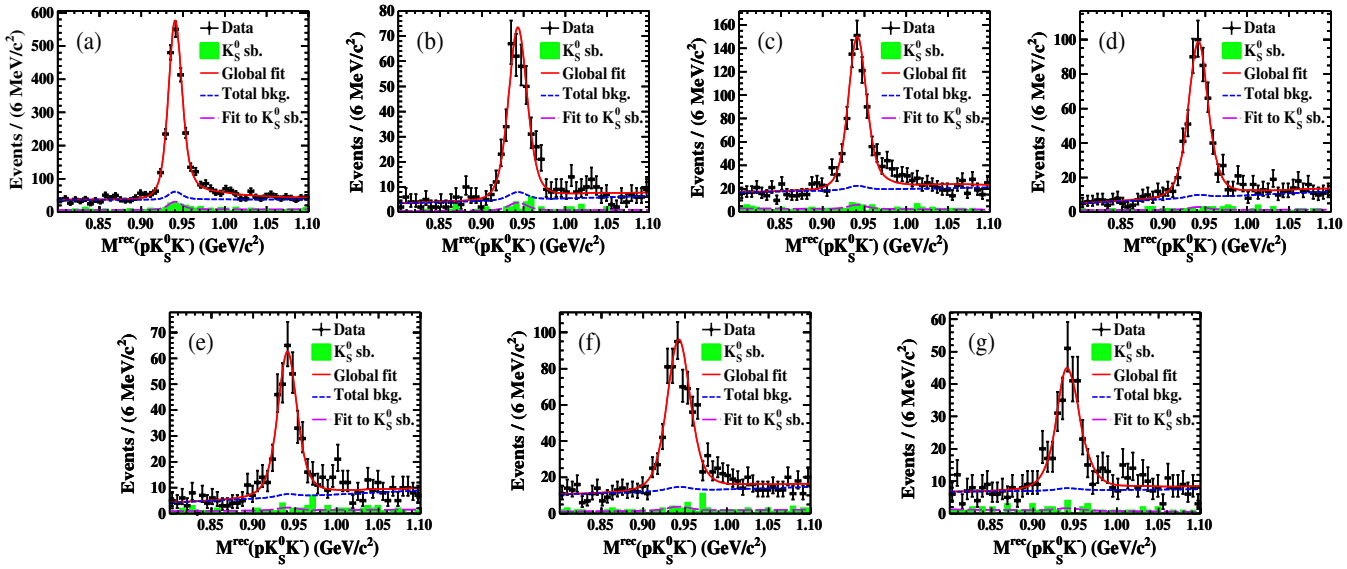

FIG. 1. Projections of the simultaneous fits to the $M^{\rm rec}(pK^0_SK^-)$ spectra and K^0_S mass sideband events in $e^+e^- \to pK^0_S\bar{n}K^-$ at c.m. energies of (a) 3.773, (b) 4.008, (c) 4.226, (d) 4.258, (e) 4.358, (f) 4.416, and (g) 4.600 GeV. The dots with uncertainty bars are the signal candidate events in data, and the green-shaded histograms are shown as the normalized K^0_S mass sideband events in data. The red solid curves show the total fits, the blue dashed lines are the total background components of the fits, and the violet long dashed curves are the fits to K^0_S mass sideband events.

c.m. energy, E_i is the energy of the ith track, and $\sum \vec{P}_i$ is the vector sum of the track momenta. For signal candidate events, the distribution of $M^{\rm rec}$ peaks at the $\bar{n}$ nominal mass [25].

Events with at least two positively charged tracks and two negatively charged tracks are selected. All charged tracks must be well reconstructed in the MDC with $|\cos\theta| < 0.93$, where θ is the polar angle between the charged track and the positron beam direction.

The K^0_S candidate is reconstructed with a pair of oppositely charged pions, where the point of the closest approach to the e^+e^- interaction point is required to be within ± 20 cm in the beam direction. A charged track is identified as a pion by using the combined TOF and dE/dx information. To suppress random combinatorial backgrounds, we require that the $\pi^+\pi^-$ pair satisfies a secondary vertex fit [28], and the decay length, which is the distance between production and decay vertexes, is required to be greater than twice its resolution. If there is more than one $\pi^+\pi^-$ combination in an event, the one with the smallest χ^2 of the secondary vertex fit is retained. A K^0_S signal is required to have the $\pi^+\pi^-$ invariant mass within $|M_{\pi^+\pi^-} - m_{K^0_S}| \le 10$ MeV/c^2, where $m_{K^0_S}$ is the K^0_S nominal mass [25].

After the selection of the two π tracks from K^0_S decays, the remaining charged tracks are assumed to be p or K, and the point of closest approach of these tracks to the e^+e^- interaction point must be within ± 10 cm in the beam direction and within 1 cm in the plane perpendicular to the beam. The net charge of the p and K combination must be zero, and multiple combinations of p and K are permitted.

A. $pK^0_S\bar{n}K^-$ mode

If multiple pK^- combinations are found, the $\bar{n}$ candidate whose $M^{\rm rec}(pK^0_SK^-)$ is closest to the world average antineutron mass value [25] is selected. After the above event selection criteria applied, a clear $\bar{n}$ signal is observed in the $M^{\rm rec}(pK^0_SK^-)$ at each c.m. energy, as shown in Fig. 1.

To investigate non-K^0_S backgrounds, the K^0_S mass sideband regions are selected as $0.4676 < M_{\pi^+\pi^-} < 0.4776$ GeV/c^2 or $0.5176 < M_{\pi^+\pi^-} < 0.5276$ GeV/c^2. According to the analysis of the inclusive MC samples in the K^0_S mass sideband regions, the main backgrounds are from many processes with the $pK^-\pi^+\pi^-\bar{n}$ final state with one weakly decaying hyperon like Λ or Σ involved, where a small peak exists, as shown in Fig. 1 in the shaded histograms. Other background events, which form a smooth distribution in the $M^{\rm rec}(pK^-K^0_S)$ spectra around 0.94 GeV/c^2, are from numerous other processes, but none of them is dominant.

At each c.m. energy, an unbinned maximum likelihood fit to the $M^{\rm rec}(pK^0_SK^-)$ spectra is performed to determine the signal and background yields in the selected candidates within $[0.80, 1.10]$ GeV/c^2 and the normalized K^0_S mass sideband events. The $\bar{n}$ signal shape is obtained through the MC simulation at each c.m. energy smeared with a Gaussian function to account for the difference in the resolution between the data and the MC simulation. The same $\bar{n}$ line shape is used for K^0_S mass sideband events, and the other, nonpeaking background contribution is described by a first-order polynomial function. Another first-order polynomial function associated with the function of the fit to K^0_S sidebands represents the remaining background

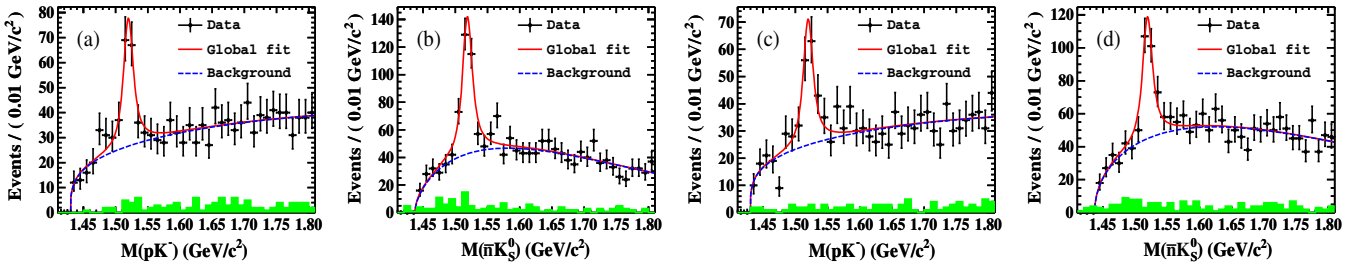

FIG. 2. Fits to the pK^- and $\bar{n}K^0_S$ invariant mass distributions to determine signal yields for $e^+e^- \to \Lambda(1520)\bar{n}K^0_S$ and $e^+e^- \to pK^-\bar{\Lambda}(1520)$, respectively, where (a) and (b) are from the data at the c.m. energy of 3.773 GeV, and (c) and (d) are from the full XYZ data. Clear $\Lambda(1520)$ signals are observed. The red solid lines show the global fits, and the blue dashed curves show the total fitted backgrounds with and without $pK^-\bar{n}K^0_S$ final states. The green-shaded histograms are the contributions of the normalized K^0_S mass sideband events in data.

contribution. The parameters of the Gaussian function and the two first-order polynomials are left free. The fits of the $M^{\rm rec}(pK^0_SK^-)$ spectra at the seven c.m. energies are shown in Fig. 1, and the signal yields along with other numerical results are summarized in Table I.

B. $\Lambda(1520)$ modes

In addition to the common selection criteria for p or K candidates, the combined TOF and dE/dx information is used to calculate $\chi^2_{\rm PID}(i)(i = p, K)$ for each hadron (i) hypothesis, and a one-constraint (1C) kinematic fit is performed with the p, K^0_S, K^-, and $\bar{n}$ combination by constraining the missing mass of the undetected $\bar{n}$ to its nominal mass [25]. The combination with the minimum $\chi^2_{\rm sum} = \chi^2_{1C} + \chi^2_{\rm PID}(p) + \chi^2_{\rm PID}(K^-)$ in an event is selected, and we require $\chi^2_{\rm sum} < 20$, where χ^2_{1C} is the χ^2 of the kinematic fit.

After the event selection requirements have been applied, clear $\Lambda(1520)$ signals are found for the processes $e^+e^- \to \Lambda(1520)\bar{n}K^0_S$ and $e^+e^- \to \Lambda(1520)\bar{p}K^+$ in data at the c.m. energy of 3.773 GeV and in the full XYZ data, as shown in Fig. 2.

According to the analysis of the inclusive MC samples, the dominant background events are from processes with $pK^0_S\bar{n}K^-$ final states without a $\Lambda(1520)$. The remaining backgrounds are from many processes with only a few events in each mode. No peaking background is found in the pK^- or nK^0_S invariant mass spectra at around 1520 MeV/c^2.

An unbinned maximum likelihood fit is performed to the pK^- and nK^0_S invariant mass distributions to determine the $\Lambda(1520)$ yields individually. The $\Lambda(1520)$ signal is described by a D-wave relativistic Breit-Wigner (BW) function with an energy-dependent width Γ_{pK} convolved with a Gaussian function. The $\Lambda(1520)$ mass and width are fixed to the world average values [25]. The pK^- and nK^0_S mass resolutions of the signal Gaussian functions are the same and fixed to 3 MeV/c^2 as determined from fits to the individual MC distributions. The background shape is parametrized by an ARGUS function [29].

For $\Lambda(1520) \to pK^-$ (the same for $\Lambda(1520) \to nK^0_S$), Γ_{pK} [30] is described by:

$$\Gamma_{pK} = \Gamma_r \left(\frac{P_{pK}}{P_r}\right)^{2L+1} \left(\frac{M_r}{M_{pK}}\right) F_r^2, \quad (1)$$

where M_{pK} is the pK invariant mass, M_r the $\Lambda(1520)$ nominal mass [25], P_{pK} the momentum of the daughter particle p or K in the pK rest frame (P_r when the pK invariant mass is the $\Lambda(1520)$ nominal mass [25]), L the $\Lambda(1520)$ decay orbital angular momentum, Γ_r the $\Lambda(1520)$ nominal width [25], and F_r the Blatt-Weisskopf penetration form factor. For $\Lambda(1520) \to pK^-$ and nK^0_S decays ($L = 2$), $F_r = \sqrt{9+3R^2P_r^2+R^4P_r^4}/\sqrt{9+3R^2P_{pK}^2+R^4P_{pK}^4}$, where R is a phenomenological factor with little sensitivity to the Γ_{pK} and generally taken as $R = 5$ GeV^{-1} [30].

To avoid double counting from $e^+e^- \to \Lambda(1520)\bar{\Lambda}\times(1520)$ in calculating the Born cross sections of $e^+e^- \to \Lambda(1520)\bar{n}K^0_S$ and $\Lambda(1520)\bar{p}K^+$, $\Lambda(1520)\bar{\Lambda}(1520)$ pair events are subtracted from the three-body decays, since it is difficult to perform a two-dimensional (2D) fit in the full range. The final number of the signal events and the corresponding statistical significance of the $e^+e^- \to \Lambda(1520)\bar{n}K^0_S$ and $\Lambda(1520)\bar{p}K^+$ signal at each c.m. energy are listed in Table II. The statistical significance is calculated using $\sqrt{-2\ln(\mathcal{L}_0/\mathcal{L}_{\rm max})}$, where $\mathcal{L}_{\rm max}$ and $\mathcal{L}_0$ are the likelihoods of the fits with and without the $\Lambda(1520)$ signal included, respectively.

We extend the unbinned maximum likelihood fit described above into a 2D fit to the pK^- versus $\bar{n}K^0_S$ mass spectra to determine the yield of the process $e^+e^- \to \Lambda(1520)\bar{\Lambda}(1520) \to pK^-\bar{n}K^0_S$. We assume that the two discriminating variables $M(pK^-)$ and $M(nK^0_S)$ are uncorrelated, and the 2D probability density function (PDF) is the product of two one-dimensional (1D) PDFs for the two variables. The total PDFs include four components: $\Lambda(1520)\bar{\Lambda}(1520)$, $\Lambda(1520)\bar{n}K^0_S$, $pK^-\bar{\Lambda}(1520)$, and non–$\Lambda(1520)$. The signal shapes of $\Lambda(1520)(\to pK^-)$

TABLE II. The c.m. energy ($\sqrt{s}$), integrated luminosity ($\mathcal{L}$), detection efficiency (ϵ), vacuum polarization ($\frac{1}{|1-\Pi|^2}$), radiative correction factor ($1+\delta$), number of observed signal events ($N_{\rm sig}$), statistical signal significance (S), and calculated (90% C.L. upper limit of) Born cross section ($\sigma_{\rm B}$) are listed for the studied $\Lambda(1520)$ modes at each energy point. The first uncertainties are statistical and the second systematic. For the 90% C.L. upper limits, the systematic uncertainties have been included.

Mode	$\sqrt{s}$ (GeV)	$\mathcal{L}$ (pb^{-1})	ϵ (%)	$\frac{1}{\lvert 1-\Pi\rvert^2}$	$1+\delta$	$N_{\rm sig}$	S (σ)	$\sigma_{\rm B}$ (pb)
$\Lambda(1520)\bar{n}K^0_S$	3.773	2931.8	23.87	1.057	0.878	122 ± 21	8.3	$1.21 \pm 0.21 \pm 0.09$
	4.008	482.0	24.64	1.044	0.927	24.7 ± 9.0	3.5	$1.38 \pm 0.50 \pm 0.10$
	4.226	1047.3	25.34	1.056	0.933	20.5 ± 9.4	3.1	$0.50 \pm 0.23 \pm 0.04$
	4.258	825.7	25.44	1.054	0.936	21.0 ± 7.8	3.3	$0.65 \pm 0.24 \pm 0.04$
	4.358	539.8	25.76	1.051	0.954	8.3 ± 5.9	3.0	$0.38 \pm 0.27 \pm 0.03$
	4.416	1028.9	25.95	1.053	0.962	25.5 ± 8.7	4.0	$0.61 \pm 0.21 \pm 0.04$
	4.600	566.9	26.53	1.055	0.970	10.3 ± 6.1	4.0	$0.43 \pm 0.25 \pm 0.03$
$\Lambda(1520)\bar{p}K^+$	3.773	2931.8	27.22	1.057	0.879	250 ± 27	11.9	$4.33 \pm 0.47 \pm 0.28$
	4.008	482.0	27.33	1.044	0.931	40 ± 11	4.3	$4.01 \pm 1.10 \pm 0.27$
	4.226	1047.3	27.45	1.056	0.935	60 ± 14	5.6	$2.72 \pm 0.63 \pm 0.18$
	4.258	825.7	27.46	1.054	0.936	24.9 ± 8.7	3.9	$1.43 \pm 0.50 \pm 0.10$
	4.358	539.8	27.51	1.051	0.951	16.1 ± 8.1	3.1	$1.39 \pm 0.70 \pm 0.10$
	4.416	1028.9	27.54	1.053	0.957	46 ± 12	4.5	$2.07 \pm 0.54 \pm 0.14$
	4.600	566.9	27.63	1.055	0.974	6.4 ± 6.8	3.0	$0.51 \pm 0.54 \pm 0.04$
$\Lambda(1520)\bar{\Lambda}(1520)$	3.773	2931.8	27.65	1.057	0.882	$< 24 (13.9 \pm 7.5)$	2.1	< 1.9
	4.008	482.0	28.77	1.044	0.928	$< 5.5 (0.0 \pm 3.5)$	0.1	< 2.4
	4.226	1047.3	29.81	1.056	0.932	$< 7.5 (1.6 \pm 3.8)$	0.5	< 1.4
	4.258	825.7	29.95	1.054	0.939	$< 7.7 (2.4 \pm 2.0)$	1.6	< 1.8
	4.358	539.8	30.42	1.051	0.954	$< 2.8 (0.0 \pm 0.8)$	0.3	< 1.0
	4.416	1028.9	30.71	1.053	0.956	$< 5.3 (0.3 \pm 2.9)$	0.1	< 1.0
	4.600	566.9	31.55	1.055	0.970	$< 2.4 (0.0 \pm 0.8)$	0.1	< 0.8

and $\bar{\Lambda}(1520)(\to \bar{n}K^0_S)$ in the 2D fit are the same as those in $e^+e^- \to \Lambda(1520)\bar{n}K^0_S$ and $\Lambda(1520)\bar{p}K^+$, respectively. All of the backgrounds are parametrized by an ARGUS function [29]. The projections of the 2D fits in data at the c.m. energy of 3.773 GeV and in the full XYZ data are shown in Figs. 3(a)–3(d).

Since only a few $\Lambda(1520)\bar{\Lambda}(1520)$ pair signal events are observed and the statistical significance is less than 3.0 standard deviations (σ) at each c.m. energy, the upper limit on the number of signal events, $N^{\rm up}_{\rm sig}$, is determined at the 90% confidence level (C.L.) by solving

$$\int_0^{N^{\rm up}_{\rm sig}} \mathcal{L}(x)dx \Big/ \int_0^{+\infty} \mathcal{L}(x)dx = 0.9, \tag{2}$$

where x is the number of fitted signal events, and $\mathcal{L}(x)$ is the likelihood function in the fit to data.

To account for the systematic uncertainties, the likelihood distribution is convolved with a Gaussian function $G(x;0,\sigma)$ with a standard deviation of $\sigma = x \times \Delta$,

$$\mathcal{L}'(\mu) = \int_0^{+\infty} \mathcal{L}(x) \times G(\mu - x; 0, \sigma)dx, \tag{3}$$

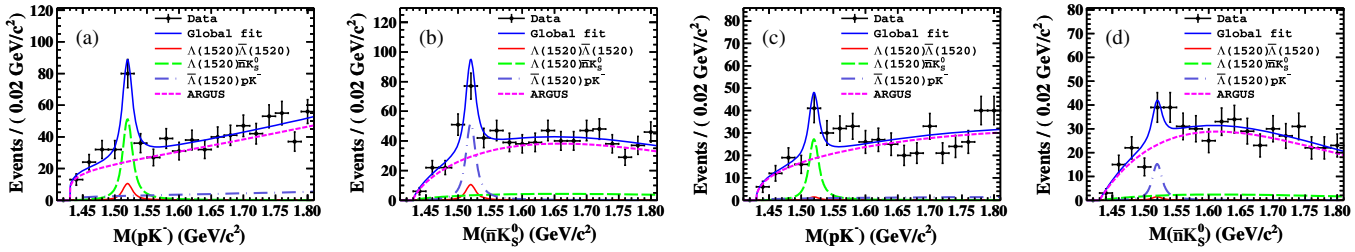

FIG. 3. Projections of the 2D fits described in the text to the $M(pK^-)$ and $M(\bar{n}K^0_S)$ distributions, where (a) and (b) are from the data at the c.m. energy of 3.773 GeV, and (c) and (d) are from the full XYZ data. The blue solid lines show the best fits, the red solid lines show the $e^+e^- \to \Lambda(1520)\bar{\Lambda}(1520)$ signals, the pink dashed lines represent the fitted non-resonant backgrounds, the gray-blue long dot-dashed lines show the contributions from $e^+e^- \to \Lambda(1520)\bar{p}K^+$, and the green long dashed lines indicate the contributions from $e^+e^- \to \Lambda(1520)\bar{n}K^0_S$.

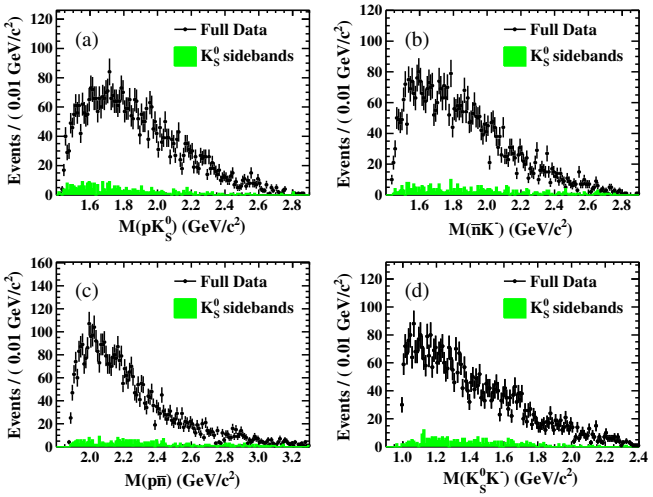

FIG. 4. Invariant mass distributions of (a) pK^0_S, (b) $\bar{n}K^-$, (c) $p\bar{n}$ and (d) $K^0_S K^-$. The dots with error bars show the full experimental data, the green shaded histograms are the contributions from the normalized K^0_S mass sidebands events.

where μ is the expected number of signal events, $\mathcal{L}'(\mu)$ indicates the expected likelihood distribution, and Δ refers to the total relative systematic uncertainty discussed in Sec. V. The upper limit on the number of $\Lambda(1520)\bar{\Lambda}(1520)$ pair events and statistical significance at each energy are listed in Table II.

To investigate other two-body invariant mass distributions, we apply the further requirement $|M(pK^-/nK^0_S) - 1.5195| > 0.025$ GeV/c^2 to veto the $\Lambda(1520)$ resonance. The pK^0_S, nK^+, $p\bar{n}$ and $K^0_S K^-$ invariant mass spectra in the full data are shown in Figs. 4(a)–4(d). No significant structures are visible.

IV. CROSS SECTION MEASUREMENT

The Born cross section is calculated using:

$$\sigma_{\rm B} = \frac{N_{\rm sig}}{\mathcal{L}_{\rm int}(1+\delta)\frac{1}{|1-\Pi|^2}\epsilon\mathcal{B}}, \quad (4)$$

where $N_{\rm sig}$ is the number of signal events, $\mathcal{L}_{\rm int}$ is the integrated luminosity, $1+\delta$ is the radiative correction factor obtained from a QED calculation with 1% accuracy [31], $\frac{1}{|1-\Pi|^2}$ is the vacuum polarization factor [32,33], ϵ is the detection efficiency from the PHSP MC simulation, $\mathcal{B}$ is the product of intermediate branching fractions, i.e., $\mathcal{B}(K^0_S \to \pi^+\pi^-)$ for $e^+e^- \to pK^0_S\bar{n}K^-$, $\mathcal{B}[\Lambda(1520) \to pK^-/nK^0_S] \times \mathcal{B}(K^0_S \to \pi^+\pi^-)$ for $e^+e^- \to \Lambda(1520)\bar{n}K^0_S/\bar{p}K^+$, and $\mathcal{B}[\Lambda(1520) \to pK^-] \times \mathcal{B}[\bar{\Lambda}(1520) \to \bar{n}K^0_S] \times \mathcal{B}(K^0_S \to \pi^+\pi^-)$ for $e^+e^- \to \Lambda(1520)\bar{\Lambda}(1520)$. The branching fractions $\mathcal{B}(K^0_S \to \pi^+\pi^-)$, $\mathcal{B}[\Lambda(1520) \to pK^-]$, and $\mathcal{B}[\Lambda(1520) \to nK^0_S]$ are 0.692, 0.225, and 0.1125 [25], respectively. All calculated Born cross sections or the 90% C.L. upper limits on the Born cross sections are summarized in Table I for the $pK^0_S\bar{n}K^-$ mode and Table II for the $\Lambda(1520)$ modes.

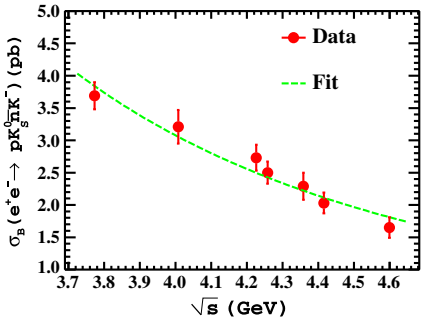

FIG. 5. Distribution of $\sigma_{\rm B}(e^+e^- \to pK^0_S\bar{n}K^-)$ versus c.m. energy. The dots with error bars, which show the sum in quadrature of the statistical and uncorrelated systematic uncertainties described in Sec. V, represent data. The dashed line shows the fit result.

The Born cross sections of $e^+e^- \to pK^0_S\bar{n}K^-$ are shown in Fig. 5 at c.m. energies between 3.773 and 4.6 GeV. We fit the $1/s^k$ dependence of the cross sections, as shown in Fig. 5 with a dashed line. The fit gives $k = 1.9 \pm 0.1 \pm 0.2$ with the goodness of the fit $\chi^2/ndf = 3.8/5$, where the first uncertainty is statistical and the second systematic.

The distributions of $\sigma[e^+e^- \to \Lambda(1520)\bar{n}K^0_S] \times \mathcal{B}[\Lambda(1520) \to pK^-]$ and $\sigma[e^+e^- \to \Lambda(1520)\bar{p}K^+] \times \mathcal{B}[\Lambda(1520) \to nK^0_S]$ versus c.m. energy are shown in Fig. 6. A fit with the functional form σ^0/s^k to each measured Born cross section is performed, as shown in Fig. 6 with the dashed lines, where σ^0 is a constant and k is a free parameter. The fits yield $k = 2.8 \pm 0.9 \pm 0.2$ ($\chi^2/ndf = 2.0/5$) and $3.5 \pm 0.6 \pm 0.2$ ($\chi^2/ndf = 5.6/5$) for the Born cross sections of $e^+e^- \to \Lambda(1520)\bar{n}K^0_S$ and $e^+e^- \to \Lambda(1520)\bar{p}K^+$, respectively, where the first uncertainties are statistical and the second systematic.

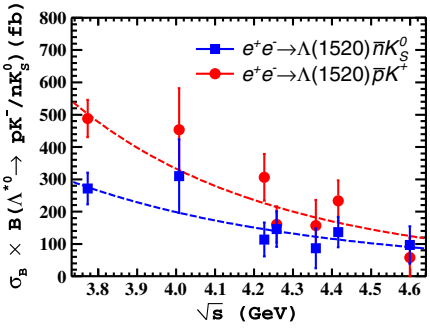

FIG. 6. (Distributions of $\sigma_{\rm B}[e^+e^- \to \Lambda(1520)\bar{n}K^0_S] \times \mathcal{B}[\Lambda(1520) \to pK^-]$, and $\sigma_{\rm B}[e^+e^- \to \Lambda(1520)\bar{p}K^+] \times \mathcal{B}[\Lambda(1520) \to nK^0_S]$ versus c.m. energy. The dots with error bars, which are the combined statistical and uncorrelated systematic uncertainties described in Sec. V, represent data. The blue and red dashed lines are the fits to the cross sections of $e^+e^- \to \Lambda(1520)\bar{n}K^0_S$ and $e^+e^- \to \Lambda(1520)\bar{p}K^+$, respectively.

V. SYSTEMATIC UNCERTAINTIES FOR BORN CROSS SECTIONS

Sources of systematic uncertainties considered in the cross-section measurements are the integrated luminosity measurement, tracking, PID, K_S^0 reconstruction, K_S^0 mass window, kinematic fit for the $\Lambda(1520)$ modes, MC generator, fitting procedure, radiative correction, vacuum polarization, and decays of intermediate states. The systematic uncertainties from the different sources for all modes are summarized in Table III, and the total systematic uncertainty is obtained by adding all contributions in quadrature assuming that each source is independent. Detailed descriptions of the estimates of the systematic uncertainties are listed in the following subsections.

A. Integrated luminosity, tracking, and PID

The luminosity is measured using large-angle Bhabha scattering events with a total uncertainty of less than 1.0% [14–16], which is taken as its systematic uncertainty at each c.m. energy.

Using the control samples of $e^+e^- \to p\bar{p}\pi^+\pi^-$ at $\sqrt{s} > 4$ GeV and $J/\psi \to K_S^0 K^\pm \pi^\mp$ events, the tracking efficiency difference between MC simulation and data is found to be 2.0% for each proton and 1.0% for each kaon. Not counting the two charged pions from K_S^0 decays, there are two charged tracks (p, K), and the uncertainty in the tracking efficiency is 3.0%.

Based on the measurements of the particle identification efficiencies of protons from $e^+e^- \to p\bar{p}\pi^+\pi^-$ events and kaons from $e^+e^- \to K^+K^-\pi^+\pi^-$ events, the difference between data and MC simulation yields uncertainties of 1.0% for each proton and 2.0% for each kaon. Thus, a total uncertainty associated with the PID of 3.0% is assigned for the $\Lambda(1520)$ modes.

B. K_S^0 reconstruction and K_S^0 mass window

The K_S^0 reconstruction efficiency is studied using two control samples: $J/\psi \to K^*(892)^\pm K^\mp \to K_S^0\pi^\pm K^\mp$ and $J/\psi \to \phi K_S^0 K^\pm \pi^\mp$. The difference in the K_S^0 reconstruction efficiency between the MC simulation and the data is 1.2% [34]. Considering the additional PID requirements for two opposite-charged pions from K_S^0 decays in our analysis, the systematic uncertainty for K_S^0 reconstruction is conservatively taken as 2.3%, where the PID efficiency difference of 1% for each pion between MC and data is included [35].

The uncertainty attributed to the K_S^0 mass window requirement, which originates from the mass resolution difference between the data and the MC simulation, is

TABLE III. Systematic uncertainties (%) in the $e^+e^- \to pK_S^0\bar{n}K^-$, $\Lambda(1520)\bar{n}K_S^0$, $\Lambda(1520)\bar{p}K^+$, and $\Lambda(1520)\bar{\Lambda}(1520)$ cross-section measurements.

$\sqrt{s}$ (GeV)		3.773	4.008	4.226	4.258	4.358	4.416	4.600
Luminosity		0.5	1.0	1.0	1.0	1.0	1.0	1.0
Tracking		3.0	3.0	3.0	3.0	3.0	3.0	3.0
PID [for $\Lambda(1520)$ modes]		3.0	3.0	3.0	3.0	3.0	3.0	3.0
K_S^0 reconstruction		2.3	2.3	2.3	2.3	2.3	2.3	2.3
K_S^0 mass window	$pK_S^0\bar{n}K^-$ mode	1.5	1.5	1.5	1.5	1.5	1.5	1.5
	$\Lambda(1520)$ modes	0.8	0.8	0.8	0.8	0.8	0.8	0.8
1C kinematic fit [for $\Lambda(1520)$ modes]		1.3	1.3	1.2	1.2	1.3	1.3	1.4
MC generator	$\Lambda(1520)\bar{n}K_S^0$	3.3	3.3	3.3	3.3	3.3	3.3	3.3
	$\Lambda(1520)\bar{p}K^+$	1.5	1.5	1.5	1.5	1.5	1.5	1.5
	$\Lambda(1520)\bar{\Lambda}(1520)$	5.5	5.5	5.5	5.5	5.5	5.5	5.5
Fit procedure	$pK_S^0\bar{n}K^-$	3.1	2.8	2.9	3.1	2.9	3.4	2.8
	$\Lambda(1520)\bar{n}K_S^0$	2.4	2.0	2.0	2.0	2.0	2.0	2.0
	$\Lambda(1520)\bar{p}K^+$	2.5	3.1	3.1	3.1	3.1	3.1	3.1
	$\Lambda(1520)\bar{\Lambda}(1520)$	4.4	3.9	3.9	3.9	3.9	3.9	3.9
Radiative correction	$pK_S^0\bar{n}K^-$ mode	1.9	1.6	1.3	1.3	1.4	1.7	1.3
	$\Lambda(1520)$ modes	1.6	1.2	1.5	1.4	1.9	1.8	2.0
Intermediate decay [for $\Lambda(1520)$ modes]		2.2	2.2	2.2	2.2	2.2	2.2	2.2
Total	$pK_S^0\bar{n}K^-$	5.5	5.3	5.3	5.4	5.3	5.7	5.2
	$\Lambda(1520)\bar{n}K_S^0$	7.1	6.9	7.0	6.9	7.1	7.0	7.1
	$\Lambda(1520)\bar{p}K^+$	6.5	6.7	6.7	6.7	6.9	6.8	6.9
	$\Lambda(1520)\bar{\Lambda}(1520)$	9.1	8.9	8.9	8.9	9.0	9.0	9.0

estimated using $|\varepsilon_{\rm data}-\varepsilon_{\rm MC}|/\varepsilon_{\rm data}$, where $\varepsilon_{\rm data}$ is the efficiency of applying the K_S^0 mass window requirement by extracting K_S^0 signal in the $\pi^+\pi^-$ invariant mass spectrum of the data at each c.m. energy, and $\varepsilon_{\rm MC}$ is the analogous efficiency from the MC simulation. The difference between the data and the MC simulation is considered as the systematic uncertainty at each c.m. energy.

C. Kinematic fit and MC generator

A correction is applied to the track helix parameters in the MC simulation to make the χ^2 distribution of the 1C kinematic fit from the MC simulation agree better with data [36]. The difference between the efficiencies with and without the correction is taken as the systematic uncertainty. In this analysis, the detection efficiencies from the MC samples with the corrected track helix parameters are taken as nominal results.

The detection efficiencies are obtained from the PHSP MC samples for $e^+e^-\to\Lambda(1520)\bar{n}K_S^0$ and $\Lambda(1520)\bar{p}K^+$. To estimate the uncertainty attributed to the MC generator, we determine the efficiency correction factor by comparing the Dalitz plots between the data and the MC simulation at the c.m. energy of 3.773 GeV, and the correction factor is assigned to the other c.m. energies due to the limited statistics. The relative differences in the efficiency with and without correction are 3.3% and 1.5% for $e^+e^-\to\Lambda(1520)\bar{n}K_S^0$ and $e^+e^-\to\Lambda(1520)\bar{p}K^+$, respectively, which are taken as the systematic uncertainties due to the MC generator at all of c.m. energies.

For $e^+e^-\to\Lambda(1520)\bar{\Lambda}(1520)$, different MC samples with angular distributions of $1+\cos^2\theta$ and $1-\cos^2\theta$ are generated, where θ is the polar angle of $\Lambda(1520)$ in e^+e^- c.m. frame. The largest difference of 5.5%, compared to the PHSP MC efficiency, is taken as the systematic uncertainty attributed to the MC generator.

D. Fit procedure

Signal yields are determined from the fits to the $M^{\rm rec}(pK_S^0K^-)$ spectra for the $pK_S^0\bar{n}K^-$ mode and the $M(pK^-)$ or $M(nK_S^0)$ spectra for $\Lambda(1520)$ modes. Alternative signal and background shapes as well as multiple fit ranges are used to estimate the systematic uncertainty in the fit procedure. We generated simulated pseudoexperiments out of the fit to the data with alternative shapes and fitted them back using the nominal model. Any deviation of the pull distributions from the normal gives the systematic effect.

1. $pK_S^0\bar{n}K^-$ mode

(1) *Signal shape:* In the nominal fit, the $\bar{n}$ signal shape is obtained from the MC simulation directly convolved with a Gaussian function. Alternatively, the incoherent sum of a Gaussian function and a Novosibirsk function [37] is taken as the $\bar{n}$ signal shape.

(2) *Background shape:* The background shape without K_S^0 mass sideband events is described by a first-order polynomial function in the nominal fit, and a second-order polynomial function is used to estimate the systematic uncertainty due to background shape.

(3) *Fit range:* In the nominal fit, the fit range is $[0.80, 1.10]$ GeV/c^2. The largest difference between the nominal fit and the fit with ranges varied to $[0.805, 1.095]$ or $[0.795, 1.115]$ GeV/c^2 is taken as the systematic uncertainty due to the fitting range.

Assuming that all of the above sources are independent, the systematic uncertainties associated with the fit procedure are the quadrature sum of above three sources.

2. $\Lambda(1520)$ modes

Since only a few $\Lambda(1520)$ signal events are observed in each $\Lambda(1520)$ mode at each c.m. energy in the XYZ data, we use the full XYZ data to estimate the uncertainty associated with the fit procedure for each XYZ data sample.

(1) *Signal shape:* In the nominal fit, the $\Lambda(1520)$ signal is described by a D-wave relativistic BW function convolved with a Gaussian function. Alternatively, the $\Lambda(1520)$ signal shape is obtained from the signal MC simulated shape convolved with a Gaussian function.

(2) *Background shape:* In the nominal fit, the background shape is described by an ARGUS function [29]. To estimate the uncertainty due to background shape, we use the alternative parametrized exponential function

$$f(M)=\begin{cases}0, & M<M_0\\ (M-M_0)^p e^{c_1(M-M_0)+c_2(M-M_0)^2}, & M\geq M_0\end{cases} \tag{5}$$

as the background shape, where M_0 is the threshold limit of the mass distributions, and p, c_1, and c_2 are free parameters.

(3) *Fit range:* In the nominal fit, the fit range is $[1.41, 1.81]$ GeV/c^2. Changing the fit range to $[1.41, 1.79]$, $[1.41, 1.80]$, $[1.41, 1.82]$ or $[1.41, 1.83]$ GeV/c^2, the largest change of signal yields with respect to the nominal value is taken as the systematic uncertainty due to the fit range.

Assuming that all of the above sources are independent and adding them in quadrature, we obtain the systematic uncertainties associated with the fit procedure for $e^+e^-\to\Lambda(1520)\bar{n}K_S^0$, $\Lambda(1520)\bar{p}K^+$, and $\Lambda(1520)\bar{\Lambda}\times(1520)$, respectively.

E. Radiative correction, vacuum polarization and intermediate decays

The line shape of the cross section for $e^+e^- \to pK^0_S\bar{n}K^-$ affects the radiative correction factor $(1+\delta)$ and detection efficiency (ϵ). For our nominal results, the dependence of the Born cross sections on the c.m. energy are $\sigma_B \propto 1/s^{1.9}$, $1/s^{2.8}$ and $1/s^{3.5}$ for $e^+e^- \to pK^0_S\bar{n}K^-$, $\Lambda(1520)\bar{n}K^-$, and $\Lambda(1520)\bar{p}K^0_S$, respectively. The dependence is assumed to be $1/s^3$ for $e^+e^- \to \Lambda(1520)\bar{\Lambda}(1520)$ due to the limited statistics. We change the energy dependence to $1/s$ for the above processes, and the largest difference in $(1+\delta)\epsilon$ among the modes is conservatively taken as the systematic uncertainty.

The vacuum polarization factor is calculated with an uncertainty of less than 0.1% [32], which is negligible compared with other sources of uncertainties.

The uncertainties of $\mathcal{B}(\Lambda(1520) \to pK^-/nK^0_S)$ and $\mathcal{B}(K^0_S \to \pi^+\pi^-)$ are 2.2% and 0.07% [25], respectively. Therefore, the uncertainty from the decays of the intermediate states is 2.2% for $\Lambda(1520)$ modes, and is disregarded in the $pK^0_S\bar{n}K^-$ mode.

VI. SYSTEMATIC UNCERTAINTIES FOR FITS TO THE CROSS SECTION DISTRIBUTIONS

The systematic uncertainty in the measured cross section is divided into two categories: the uncorrelated part among the different c.m. energies, which comes from the fit to the $\bar{n}$ or $\Lambda(1520)$ mass spectrum to determine the signal yields, and the correlated part, which includes all other uncertainties common for the whole data set. By including the uncorrelated uncertainty in the fit to the cross section distributions, the systematic uncertainties in the parameter k are estimated to be 8.6%, 6.5%, and 4.3% for the decays of $e^+e^- \to pK^0_S\bar{n}K^-$, $\Lambda(1520)\bar{n}K^0_S$, and $\Lambda(1520)\bar{p}K^+$, respectively.

VII. SUMMARY AND DISCUSSION

In summary, we study for the first time the processes $e^+e^- \to pK^0_S\bar{n}K^-$, $\Lambda(1520)\bar{n}K^0_S$, $\Lambda(1520)\bar{p}K^+$, and $\Lambda(1520)\bar{\Lambda}(1520)$ using data samples with a total integrated luminosity of 7.4 fb^{-1} collected with the BESIII detector at c.m. energies of 3.773, 4.008, 4.226, 4.258, 4.358, 4.416, and 4.600 GeV. The Born cross sections of $e^+e^- \to pK^0_S\bar{n}K^-$ are measured, and no structure in the cross section line shape between 3.773 and 4.60 GeV is visible.

Furthermore, $\Lambda(1520)$ signals are observed in the pK^- and nK^0_S invariant mass spectra for the processes $e^+e^- \to \Lambda(1520)\bar{n}K^0_S$ and $\Lambda(1520)\bar{p}K^+$ with statistical significances equal to or greater than 3.0σ, and the corresponding Born cross sections are measured. For $e^+e^- \to \Lambda(1520)\bar{\Lambda}(1520)$, the statistical significances are less than 3.0σ, and the 90% C.L. upper limits on the Born cross sections are determined. No other significant structure is found in the pK^-, nK^0_S, pK^0_S, nK^+, $p\bar{n}$ or $K^0_SK^-$ invariant mass spectra in any of the data samples.

As a consequence, no light hadron decay modes of Y states or conventional charmonium resonances are observed in our analysis. However, we note that there is an evident difference in line shape and magnitude of the measured cross sections between $e^+e^- \to \Lambda(1520)\bar{n}K^0_S$ and $e^+e^- \to \Lambda(1520)\bar{p}K^+$ (the statistical significance of the cross-section difference is 3.1σ at the c.m. energy of 3.770 GeV). Such an isospin violating effect may be due to the interference between $I=1$ and $I=0$ final states. The final states $\Lambda(1520)\bar{n}K^0_S$ and $\Lambda(1520)\bar{p}K^+$ can be produced from pK^- and $\bar{n}K^0_S$ systems either in $I=1$ or $I=0$ states, namely, excited Σ^* or Λ^* states. These two states can decay into both pK^- and $\bar{n}K^0_S$ final states, but with a sign difference from Clebsch-Gordan coefficients. Another possible approach is $e^+e^- \to K^*\bar{K}$ with highly excited K^* decays into $\Lambda^*\bar{p}$ or $\Lambda^*\bar{n}$. The $K^*\bar{K}$ system can be produced from $I=1$ (excited ρ) or $I=0$ (excited ω or ϕ) states, where the interference effect can occur. If the final state is $p\bar{N}^*$ or $n\bar{N}^*$, a similar pattern could be observed. More experimental data are desirable to confirm these interpretations and speculations in the future.

ACKNOWLEDGMENTS

The BESIII collaboration thanks the staff of BEPCII and the IHEP computing center for their strong support. This work is supported in part by National Key Basic Research Program of China under Contract No. 2015CB856700; National Natural Science Foundation of China (NSFC) under Contracts No. 11335008, No. 11425524, No. 11625523, No. 11635010, No. 11735014, No. 11705006; the Chinese Academy of Sciences (CAS) Large-Scale Scientific Facility Program; the CAS Center for Excellence in Particle Physics (CCEPP); Joint Large-Scale Scientific Facility Funds of the NSFC and CAS under Contracts No. U1532257, No. U1532258, No. U1732263; CAS Key Research Program of Frontier Sciences under Contracts No. QYZDJ-SSW-SLH003, No. QYZDJ-SSW-SLH040; 100 Talents Program of CAS; INPAC and Shanghai Key Laboratory for Particle Physics and Cosmology; German Research Foundation DFG under Contracts Nos. Collaborative Research Center CRC 1044, FOR 2359; Istituto Nazionale di Fisica Nucleare, Italy; Koninklijke Nederlandse Akademie van Wetenschappen (KNAW) under Contract No. 530-4CDP03; Ministry of Development of Turkey under Contract No. DPT2006K-120470; National Science and Technology fund; The Swedish Research Council; U.S. Department of Energy under Contracts Nos. DE-FG02-05ER41374, DE-SC-0010118, DE-SC-0010504, DE-SC-0012069; University of Groningen (RuG) and the Helmholtzzentrum fuer Schwerionenforschung GmbH (GSI), Darmstadt.

[1] S. Godfrey and S. L. Olsen, The exotic XYZ charmonium-like mesons, Annu. Rev. Nucl. Part. Sci. **58**, 51 (2008).

[2] N. Brambilla *et al.*, Heavy quarkonium: Progress, puzzles, and opportunities, Eur. Phys. J. C **71**, 1534 (2011).

[3] N. Brambilla *et al.*, QCD and strongly coupled gauge theories: Challenges and perspectives, Eur. Phys. J. C **74**, 2981 (2014).

[4] B. Aubert *et al.* (*BABAR* Collaboration), Observation of a Broad Structure in the $\pi^+\pi^- J/\psi$ Mass Spectrum around 4.26-GeV/c^2, Phys. Rev. Lett. **95**, 142001 (2005).

[5] J. P. Lees *et al.* (*BABAR* Collaboration), Study of the reaction $e^+e^- \to J/\psi\pi^+\pi^-$ via initial-state radiation at *BABAR*, Phys. Rev. D **86**, 051102 (2012).

[6] Q. He *et al.* (CLEO Collaboration), Confirmation of the Y(4260) resonance production in ISR, Phys. Rev. D **74**, 091104 (2006).

[7] C. Z. Yuan *et al.* (Belle Collaboration), Measurement of $e^+e^- \to \pi^+\pi^- J/\psi$ Cross Section via Initial-State Radiation at Belle, Phys. Rev. Lett. **99**, 182004 (2007).

[8] M. Ablikim *et al.* (BESIII Collaboration), Observation of a Charged Charmoniumlike Structure in $e^+e^- \to \pi^+\pi^- J/\psi$ at $\sqrt{s} = 4.26$ GeV, Phys. Rev. Lett. **110**, 252001 (2013).

[9] Z. Q. Liu *et al.* (Belle Collaboration), Study of $e^+e^- \to \pi^+\pi^- J/\psi$ and Observation of a Charged Charmoniumlike State at Belle, Phys. Rev. Lett. **110**, 252002 (2013).

[10] X. H. Mo, G. Li, C. Z. Yuan, K. L. He, H. M. Hu, J. H. Hu, P. Wang, and Z. Y. Wang, Determining the upper limit of Gamma(ee) for the Y(4260), Phys. Lett. B **640**, 182 (2006).

[11] M. Ablikim *et al.* (BESIII Collaboration), Evidence of two resonant structures in the $e^+e^- \to \pi^+ D^0 D^{*-}$ cross section between 4.05 and 4.60 GeV, arXiv:1808.02847.

[12] M. Ablikim *et al.* (BESIII Collaboration), Design and construction of the BESIII detector, Nucl. Instrum. Methods Phys. Res., Sect. A **614**, 345 (2010).

[13] M. Ablikim *et al.* (BESIII Collaboration), Measurement of the center-of-mass energies at BESIII via the di-muon process, Chin. Phys. C **40**, 063001 (2016).

[14] M. Ablikim (BESIII Collaboration), Measurement of the integrated luminosities of the data taken by BESIII at $\sqrt{s} =$ 3.650 and 3.773 GeV, Chin. Phys. C **37**, 123001 (2013).

[15] M. Ablikim *et al.* (BESIII Collaboration), Measurement of the $e^+e^- \to \pi^+\pi^-$ cross section between 600 and 900 MeV using initial state radiation, Phys. Lett. B **753**, 629 (2016).

[16] M. Ablikim *et al.* (BESIII Collaboration), Precision measurement of the integrated luminosity of the data taken by BESIII at center of mass energies between 3.810 GeV and 4.600 GeV, Chin. Phys. C **39**, 093001 (2015).

[17] S. Agostinelli *et al.* (GEANT4 Collaboration), GEANT4: A simulation toolkit, Nucl. Instrum. Methods Phys. Res., Sect. A **506**, 250 (2003).

[18] Z. Y. Deng *et al.*, Object-oriented BESIII detector simulation system, Chin. Phys. C **30**, 371 (2006).

[19] P. Golonka and Z. Was, PHOTOS Monte Carlo: A precision tool for QED corrections in Z and W decays, Eur. Phys. J. C **45**, 97 (2006).

[20] R. G. Ping, An exclusive event generator for e^+e^- scan experiments, Chin. Phys. C **38**, 083001 (2014).

[21] S. Jadach, B. F. L. Ward, and Z. Was, The precision Monte Carlo event generator K K for two fermion final states in e^+e^- collisions, Comput. Phys. Commun. **130**, 260 (2000).

[22] S. Jadach, B. F. L. Ward, and Z. Was, Coherent exclusive exponentiation for precision Monte Carlo calculations, Phys. Rev. D **63**, 113009 (2001).

[23] R. G. Ping, Event generators at BESIII, Chin. Phys. C **32**, 599 (2008).

[24] D. J. Lange, The EvtGen particle decay simulation package, Nucl. Instrum. Methods Phys. Res., Sect. A **462**, 152 (2001).

[25] M. Tanabashi *et al.* (Particle Data Group), Review of particle physics, Phys. Rev. D **98**, 030001 (2018).

[26] J. C. Chen, G. S. Huang, X. R. Qi, D. H. Zhang, and Y. S. Zhu, Event generator for J/ψ and $\psi(2S)$ decay, Phys. Rev. D **62**, 034003 (2000).

[27] T. Sjöstrand, S. Ask, J. R. Christiansen, R. Corke, N. Desai, P. Ilten, S. Mrenna, S. Prestel, C. O. Rasmussen, and P. Z. Skands, An introduction to PYTHIA 8.2, Comput. Phys. Commun. **191**, 159 (2015).

[28] M. Xu *et al.*, Decay vertex reconstruction and 3-dimensional lifetime determination at BESIII, Chin. Phys. C **33**, 428 (2009).

[29] H. Albrecht *et al.* (ARGUS Collaboration), Measurement of the polarization in the decay $B \to J/\psi K*$, Phys. Lett. B **340**, 217 (1994).

[30] S. Kopp *et al.* (CLEO Collaboration), Dalitz analysis of the decay $D0 \to K - \pi^+\pi^0$, Phys. Rev. D **63**, 092001 (2001).

[31] E. A. Kuraev and V. S. Fadin, On radiative corrections to e^+e^- single photon annihilation at high-energy, Sov. J. Nucl. Phys. **41**, 466 (1985).

[32] S. Actis *et al.*, Quest for precision in hadronic cross sections at low energy: Monte Carlo tools vs. experimental data, Eur. Phys. J. C **66**, 585 (2010).

[33] F. Jegerlehner, [Online; accessed March-2018], http://www.physik.hu-berlin.de/fjeger/.

[34] M. Ablikim *et al.* (BESIII Collaboration), Study of χ_{cJ} decaying into $\phi K^*(892)\bar{K}$, Phys. Rev. D **91**, 112008 (2015).

[35] M. Ablikim *et al.* (BESIII Collaboration), Observation of a Charged $(D\bar{D}^*)^{\pm}$ Mass Peak in $e^+e^- \to \pi D\bar{D}^*$ at $\sqrt{s} = 4.26$ GeV, Phys. Rev. Lett. **112**, 022001 (2014).

[36] M. Ablikim *et al.* (BESIII Collaboration), Search for hadronic transition $\chi_{cJ} \to \eta_c\pi^+\pi^-$ and observation of $\chi_{cJ} \to K\bar{K}\pi\pi\pi$, Phys. Rev. D **87**, 012002 (2013).

[37] H. S. Ahn *et al.*, Study of characteristics of the BELLE CsI calorimeter prototype with a BINP tagged photon beam, Nucl. Instrum. Methods Phys. Res., Sect. A **410**, 179 (1998).